Optoelectronic Properties of Layered Perovskite Solar Cells

Bekele Hailegnaw, Sanghyun Paek, Kyung Taek Cho, Yonghui Lee, Fathi Ongül, Mohammad Khaja Nazeeruddin, and Markus Clark Scharber*

Herein, the optoelectronic properties of interface-engineered perovskite 2D|3D-heterojunction structure solar cells are reported. The reciprocity theorem is applied to determine the maximum open-circuit voltage (V_{oc}) the device can deliver under solar illumination. A V_{oc} of 1.295 V is found, analyzing the measured external quantum efficiency and assuming only radiative recombination. For comparison, the experimental open-circuit voltage found for the studied 2D|3D heterojunctions is 1.15 V. The contribution of nonradiative recombination is explored by measuring the electroluminescence quantum yield. A quantum yield of 0.4% is found at current densities equivalent to 1 sun illumination. This translates into a V_{oc} loss of $\approx$140 mV, which is in very good agreement with the experimental findings. In addition, the fundamental correlation between luminescence intensity and the chemical potential predicted by the generalized Planck law is confirmed for the photoluminescence measured at different light intensities when the device is operated under open-circuit conditions and for the electroluminescence when operated under a forward bias. The investigations in this study suggest that further efficiency improvements can be achieved by reducing the nonradiative recombination in the studied solar cell. At the same time, a high-performance near IR light emitting diode can be realized.

1. Introduction

Perovskite solar cells have reached power conversion efficiencies (PCEs) >23% since the first report of an organic–inorganic perovskite photovoltaic device was published in 2009.[1,2] Advantages of this type of solar cell range from inexpensive absorber materials to simple and versatile device designs and manufacturing processes. Devices can be deposited from a solution; printing of mini-modules with a good efficiency has been demonstrated,[3,4] and the realization of flexible[5,6] and semitransparent[7] devices suggests that perovskite solar cells could be suitable for various different products and applications.

B. Hailegnaw, Dr. F. Ongül, Dr. M. C. Scharber
Linz Institute of Organic Solar Cells
Johannes Kepler University Linz
Altenbergerstrasse 69, 4040 Linz, Austria
E-mail: Markus_Clark.Scharber@jku.at

Dr. S. Paek, Dr. K. T. Cho, Dr. Y. Lee, Prof. M. K. Nazeeruddin
Group for Molecular Engineering of Functional Materials
EPFL Valais Wallis
CH-1951 Sion, Switzerland

The ORCID identification number(s) for the author(s) of this article can be found under https://doi.org/10.1002/solr.201900126.

However, the commercialization of perovskite solar cells (PSCs) is still restricted by insufficient long-term stability and environmental concerns related to the use of water-soluble lead compounds. Moisture, UV radiation, and thermal stress were found to be the main degradation sources for many perovskite semiconductors especially with a 3D ABX_3 crystal structure.[8–10] One proposed strategy to improve the stability of perovskite absorbers is the use of lower-dimensional (2D) structures derived from the Ruddlesden–Popper (RP) phases. Recent experimental studies found that quasi-2D perovskites can show much better thermodynamic and chemical stabilities compared with the corresponding 3D bulk perovskites.[11] First principles calculations support these findings.[12] However, 2D perovskites have wider bandgap and large exciton binding energies, making them less suitable for photovoltaic applications.[13] Low-dimensional perovskites with 3D perovskites in layered 2D/3D composites have been proposed as a strategy to utilize the properties of both material classes, resulting in stable and high-performance perovskite-based absorber layers.[4,14] A construction of stacked 2D/3D structures can already combine the advantages of enhanced stability in 2D perovskites as well as the outstanding optoelectronic properties of 3D perovskite materials.[15] Interestingly, incorporation of the 2D perovskite layer can also reduce hysteresis, which is attributed to an increase in the interfacial charge extraction and a decrease in recombination.[16]

One-step and two-step deposition processes have been optimized to deposit 2D/3D bilayers, allowing the preparation of solar cells with a power conversion efficiency of 20%.[18] In a one-step process, the precursors for the 3D and 2D perovskite are mixed and the layers are grown simultaneously, whereas in a two-step process, the 2D perovskite is grown on top of the 3D crystal in a consecutive step.[4,14,17,18] In this article, we summarize our investigations on a two-step-processed 2D/3D perovskite photovoltaic device. The mixed cation/mixed halide absorber layer is processed from lead-rich $(FAPbI_3)_{0.85}(MAPbBr_3)_{0.15}$ and $CsPbI_3$ solution, which is deposited by spin coating. During film formation, an anti-solvent treatment is applied, and the resulting film is annealed in an inert atmosphere. This gives a high-quality perovskite layer. In a second step, phenylethylammonium iodide (PEAI) is spin-coated on the perovskite layer to obtain a 2D perovskite in the form of PEA_2PbI_4. The PEAI bulky cation has a large molecular radius that causes anionic layers in the 3D architecture

to be isolated and transformed into a 2D perovskite. With this procedure, a perovskite-based heterostructure is created with the 2D material forming a surface passivation layer of the 3D absorber layer.[18]

We study the device characteristics such as the spectral response and the emissive properties. Applying the reciprocity relation for optoelectronic devices,[19] we analyzed potential open-circuit voltage (V_{oc}) losses. The studied solar cells show a moderate electroluminescence quantum yield (ELQY) of $\approx 0.4\%$, which may already be sufficient for some applications requiring near-IR radiation. For example, a set of two identical devices could be used to probe the transmission of liquids or thin films. One device is operated as the light source, whereas the second is operated in the photodetector mode. Due to the overlap of the absorption and emission of the studied perovskite solar cells, such a device can be realized with one and the same perovskite semiconductor. Recently, more than one order of magnitude larger luminescence quantum yield have been reported for a solar cell with the MAPbI$_3$ absorber sandwiched between two organic charge transport layers and a mixed halide mixed cation perovskite passivated with polyethylammonium iodide.[20,21]

Both reports support the idea that nonradiative recombination in perovskites can be reduced by optimizing the semiconductor growth procedure, the choice of interfacial layers, and the careful passivation of surface states. Several different semiconductor deposition processes have been reported, and the purity of starting materials, temperature, and humidity of the processing environment and the timing of the different processing steps appear to be very critical. On the other hand, the formation of a surface passivation layer by applying amine-based moieties works for many different molecules and perovskite semiconductors. Enhancing the radiative recombination in the studied 2D/3D perovskite solar cells would be very beneficial. An ELQY of 5% would result in a ≈ 60 mV increase, and an open-circuit voltage >1.2 V could be achieved.

2. Results and Discussion

In **Figure 1**a, typical current–voltage curves of a 2D/3D perovskite solar cell recorded with and without illumination are shown. Under simulated AM 1.5G irradiation, solar cells typically deliver a V_{oc} of 1.15 V, a short-circuit current (EQE corrected) of ≈ 22 mA cm^{-2}, and an electrical fill factor (FF) of ≈ 0.65. The FF is lower compared with the values reported for similar devices in recent publications.[18] The wires attached to the solar cells increase the serial resistance, and a characterization without a shadow mask limiting the area exposed to solar radiation lead to additional electrical losses reducing the electrical fill factor. Figure 1b shows the external quantum efficiency spectra recorded at a normal incidence and when the solar cell is tilted by 30° with respect to the incident light. In the same figure, the reflection of the solar cell, recorded simultaneously with the EQE-spectrum at 30° tilt, is plotted. While the EQE is 80–90% in the range of 400–700 nm, the recorded reflectance is 5–10% in the same spectral range. In the near IR-region, the reflectivity of the solar cell reaches $\approx 60\%$. The recorded spectra suggest that the investigated devices are fairly optimized in the absorption region while the geometrical reflectance of the stack is reduced due to light scattering

and parasitic absorption in the electrodes or interfacial layers. In Figure 1c, the external quantum efficiency recorded over a wide spectral range and the measured and the calculated electroluminescence (EL) spectra of the same device are compared. The EQE spectrum shows a very steep onset around 1.4 eV. The EQE setup used for this experiment has a detection limit of $\approx 10^{-6}$, and the signal observed at lower energies (1–1.3 eV) is inherent to the detection system and neglected for all performed calculations. The recorded EQE spectrum can be used to calculate the emission spectrum of the device. By multiplying the EQE(E) and the emission spectrum of a blackbody radiator kept at room temperature ($\phi_{BB}(E)$), the position and the shape of the photoluminescence and electroluminescence spectra can be derived. Figure 1c shows the calculated emission spectrum (black dots) and the measured EL spectrum (red line) for comparison. The agreement between the calculated and the measured spectra is very good.

The position and the line width of photoluminescence and the electroluminescence spectra of the studied devices are identical. Figure S2, Supporting Information, compares the EL spectrum, when the solar cell is operated at 1.1 V and the PL spectrum, when the device is kept at open-circuit conditions and excited by a 532 nm laser diode (≈ 0.1 mW cm^{-2}). In Figure 1d, the EL quantum yield (ELQY) as a function of the current density is plotted. At current densities comparable with the short current density at 1 sun, the ELQY is $\approx 0.4\%$. Around 12 mA cm^{-2}, the ELQY reaches a maximum ($\approx 0.6\%$) and decreases at lower currents. Several different devices with comparable EQE-spectra and current–voltage curves did show similar ELQYs. For comparison, a solar cell based on a methylammonium lead iodide absorber layer sandwiched between thin layers of poly(3,4-ethylenedioxythiophene) polystyrene sulfonate (PEDOT:PSS) and phenyl-C$_{61}$-butyric acid methyl ester (PCBM) exhibits a electroluminescence quantum yield $<10^{-4}\%$,[22] whereas for solar cells with surface passivation, ELQY $>1\%$ has been reported recently.[20,21]

The external quantum efficiency spectrum and the electroluminescence quantum yield can be used to estimate the open-circuit voltage losses due to nonradiative recombination. The maximum open-circuit voltage, when the device is operated at room temperature and exposed to AM 1.5G radiation, is given by

$$V_{oc,rad} = \frac{k_B T}{q} \ln\left(\frac{i_{sc}}{i_o} + 1\right) \tag{1}$$

where i_0 and i_{sc} are given by

$$i_{sc} = q \int EQE(E) \times \Phi_{AM1.5G}(E)\,dE \tag{2}$$

$$i_0 = q \int EQE(E) \times \Phi_{BB}(E)dE \tag{3}$$

and q is the unit charge, k_B is the Boltzmann constant, and T is the temperature (300 K). The evaluation of the EQE spectrum shown in Figure 1c leads an open-circuit voltage of 1.295 V at the radiative limit. Voltage losses caused by the nonradiative recombination can be calculated by Equation (4).
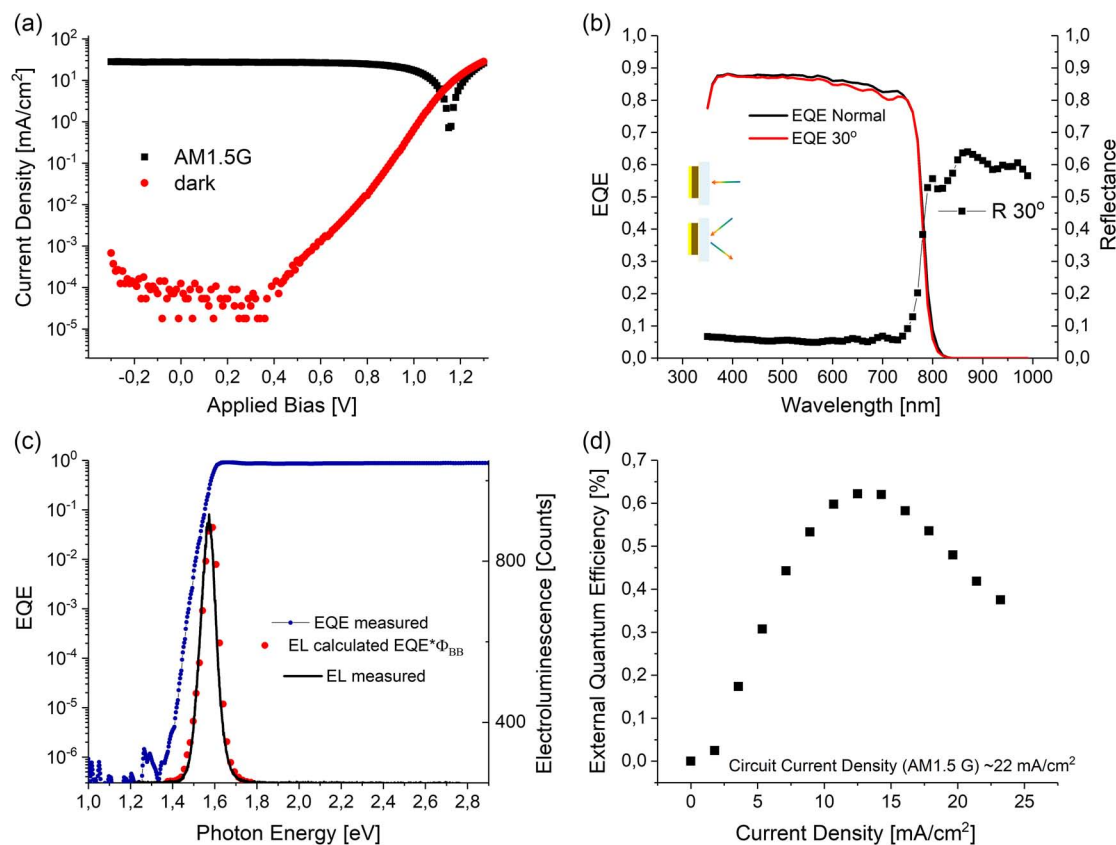
Figure 1. a) Current–voltage curves (dark and under illumination) of a 2D/3D perovskite solar cell. b) External quantum efficiency spectra and the reflectance a 2D/3D perovskite solar cell. c) External quantum efficiency and measured and calculated electroluminescence spectra. d) Electroluminescence quantum efficiency versus current density.

$$V_{oc,rad} - V_{oc} = \frac{k_B T}{e} \ln (ELQE) \qquad (4)$$

With an ELQY of 0.4%, the open-circuit voltage loss due to the nonradiative recombination is ≈ 0.14 V. This is in very good agreement with the experimental results (1.295–1.15 V = 0.145 V). The measured and calculated solar cell parameters are summarized in **Table 1**. It is interesting to note that high-performance silicon and copper indium gallium selenide (CIGS)-based solar cells exhibit similar V_{oc} losses due to nonradiative recombination. For the studied perovskite cells, a reduction of the nonradiative recombination could increase the open-circuit voltage by more than 100 mV.

In **Figure 2**a,b, the photoluminescence measured at different light intensities, while keeping the device at open circuit, and the electroluminescence at different applied potentials corrected for the potential drop at the serial resistance R_s (25 Ω) are shown.[23,24] The serial resistance was estimated by analyzing the current–voltage curves of the investigated solar cell recorded at different light intensities. A fundamental correlation between

the luminescence intensity and the open-circuit voltage is predicted by the generalized Planck equation.[25] PL should be proportional to $\exp(qV_{oc}/k_B T)$, whereas EL increases with $\exp(qV_a/k_B T)$ with V_a being the voltage drop across the semiconductor volume. In both experiments, we find an exponential dependence of the recorded emission as a function of the voltage across the solar cell. The slope is close to $q/k_B T$ for the photoluminescence and electroluminescence signals.

Deviations of the predicted slope $q/(k_B T)$ may be caused by temperature variations due to the photoexcitation (PL) or resistive heating (EL). In **Figure 3**, the bias dependence of the photoluminescence is shown. The solar cell was operated at different potentials while illuminated with a monochromatic light source.

At reverse bias and moderate forward biases, the photoluminescence signal is small. A large fraction of the photoexcited charges is extracted through the electrodes, and charge carriers do not recombine in the semiconductor. Upon applying a forward bias, a recombination current proportional to $\exp(qV/(nk_B T))$ is induced, where n is the ideality factor of the diode. Up to +600 mV, the photoluminescence increase is very moderate. At higher voltages, an exponential PL increase is observed. In this case, the slope is smaller than $e/(k_B T)$ (Figure 3c). The observation of emission even at a reverse bias suggests that isolated volumes in the perovskite layer exist, which are photovoltaically inactive. Photoexcitations in these volumes do not contribute to the
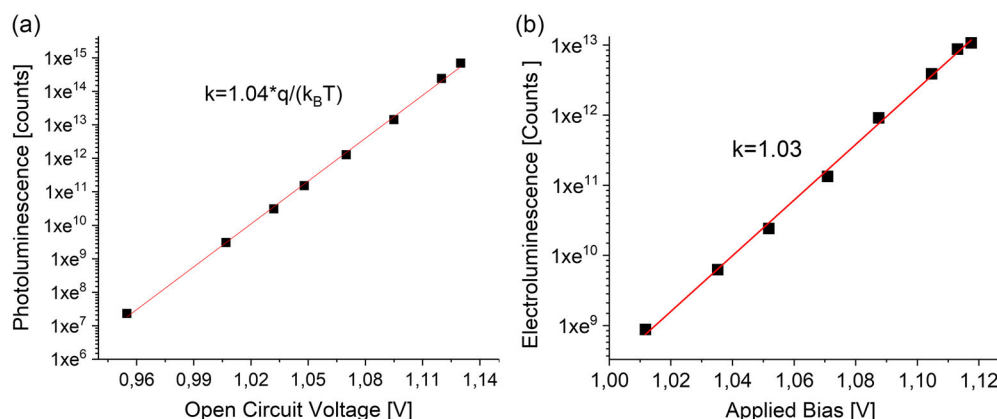
Table 1. Summary of measured and calculated solar cell parameters.

V_{oc} [V]	I_{sc} [mA cm^{-2}]	Fill factor [%]	$V_{oc,rad}$ [V]	EL quantum yield [%]
1.15	22.0	65	1.295	0.4

Figure 2. a) Photoluminescence recorded at different open-circuit voltages. b) Electroluminescence versus the voltage drop across the photovoltaic device.
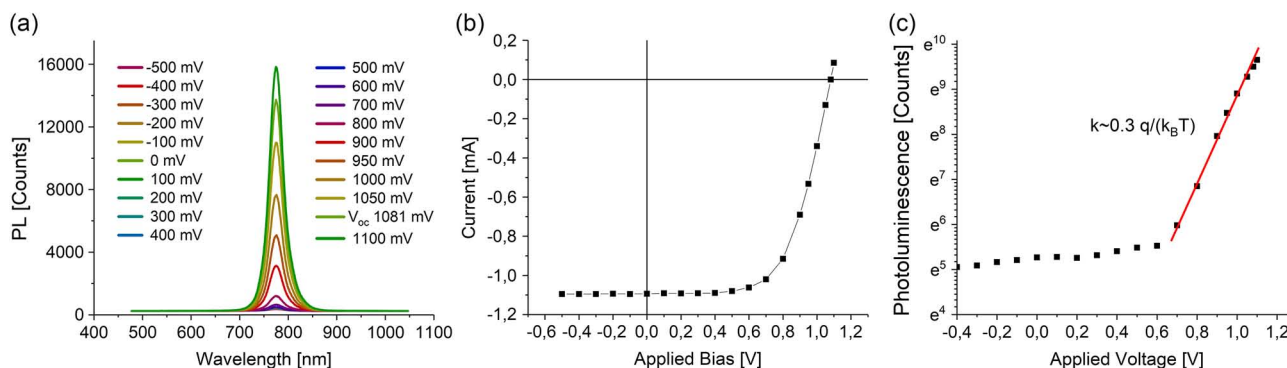

Figure 3. a) Photoluminescence spectra versus applied bias. b) Current–voltage curve. c) Photoluminescence amplitude versus applied bias.

photocurrent but need to recombine in the isolated volume, leading to a bias-insensitive component of the photoluminescence. The origin of the small slope in the bias-dependent PL experiment is still not understood. In the literature, an exponential-like variation has already been observed for CIGS or CdTe (cadmium telluride) solar cells and was explained by solving the drift-diffusion equation and calculating the local quasi Fermi level splitting in the absorber region.[26–28] Developing an advanced model for the bias-dependent luminescence of high-performance perovskite solar cells could deliver a deep inside into the effect of interlayers, contact selectivity, and defects in these devices.

3. Summary and Conclusions

The performed studies demonstrate the outstanding performance of state-of-the-art 2D/3D perovskite solar cells. A steep increase of the external quantum efficiency at the absorption onset and a relatively high radiative recombination quantum yield lead to high open-circuit voltages. By applying the reciprocity relation between the light emitting and photovoltaic properties of a solar cell, we can relate the EQE and ELQY to the open-circuit voltage of the investigated devices. Our

experiments and calculations predict that the open-circuit voltage could be about 150 mV high, if all nonradiative recombination channels can be switched off. Bias-dependent photoluminescence measurements suggest that there are disconnected volumes in the absorber layer. These volumes do not only lead to parasitic absorption but they may also hamper charge transport through the semiconductor layer. Overall, despite their excellent optoelectronic properties, there is still potential to improve the performance of the studied 2D/3D perovskite devices. Increasing the crystallinity of the absorber and optimization of the 2D capping layer could reduce the inactive absorber volume and the nonradiative recombination.

4. Experimental Section

Devices were fabricated at EPFL Sion following the procedure described below. Materials were used as received. Product names, vendors, and patch numbers are summarized in **Table 2**. Fluorine-doped tin oxide (FTO) glass substrates (Nippon sheet glass) were sequentially cleaned with the detergent solution, acetone, and ethanol. Then, by the spray pyrolysis deposition, a compact TiO_2 layer was coated on the cleaned FTO substrate heated at 450 °C. A precursor solution diluted titanium diisopropoxide

Table 2. Materials used to fabricate the studied solar cells.

Product name	Company	Catalogue number
Titanium diisopropoxide bis(acetylacetonate), 75 wt% in isopropanol	Sigma-Aldrich	325252-100ML
TBP	—	142379-25G
Li-TFSI	—	544094-25G
TiO$_2$ paste	GreatCell solar	30 NR-D
SnCl$_4$	Across	19751-1000
FAI	—	MS150000-100g
MABr	—	MS301000-100g
PEAI	—GreatCell solar	MS109200-10g
FK209	—	MS2203050
PbI$_2$	TCI	L0279
PbBr$_2$	—	L0288
CsI	ABCR	AB207757-0050.00
Spiro_OMeTAD	Merk	SHT-263
All solvent used Extra Dry, AcroSeal	Across	—

in ethanol (0.6 and 10 mL). Thereafter, a bilayer electron transport layer was prepared with mesoporous TiO$_2$ and SnO$_2$. Mesoporous TiO$_2$ films were prepared using a diluted TiO$_2$ paste solution. Films were spin-coated and sintered on a hot plate at 500 °C for 30 min. The SnO$_2$ layer was prepared by spin-coating a precursor solution of SnCl$_4$ dissolved in water. SnCl$_4$ aqueous solution (0.1 M) was spin-coated and sintered on a hot plate at 180 °C for 1 h. The lead excess Cs$_{0.1}$ (FAPbI3)$_{0.81}$(MAPbBr3)$_{0.09}$ precursor solution was prepared by mixing FAI (1.05 M), PbI2 (1.21 M), MABr (0.12 M), PbBr2 (0.12 M), and CsI (0.13 M) in a mixed solvent of dimethylformamide (DMF):dimethyl sulfoxide (DMSO) = 4:1 (volume ratio). The perovskite precursor solution was spin-coated at 2000 rpm for 10 s, followed by 5000 rpm for 30 s. Trifluorotoluene (110 μL) was dropped on the spinning substrate at 10 s in the second step. The films were annealed at 100 °C for 90 min in the glove box. For forming an additional 2D perovskite film on top of this perovskite film, cooled substrates were treated with a PEAI isopropanol solution. The PEAI solution (100 mL) (15 mg mL^{-1}) were spin-coated on the as-prepared perovskite films at 4000 rpm, which is similar to the anti-solvent dropping method. The films were annealed at 100 °C for 10 min. The hole-transporting materials were applied from a 40 mM solution in chlorobenzene. Tert-butylpyridine (tBP), tris(2-(1H-pyrazol-1-yl)-4-*tert*-butylpyridine)cobalt(III) (FK209), and tris(bis(trifluoromethylsulfon-yl)imide) (Li-TFSI) were added as additives. Equimolar amounts of additives were added for all hole transporters: 330 mol% tBP, 50 mol% Li-TFSI from a 1.8 M stock solution in acetonitrile, and 3 mol% FK209 from a 0.25 M stock solution in acetonitrile. Finally, 70 nm of Au was deposited by thermal evaporation as the back electrode resulting in solar cells with an active area of 0.65 cm^2.

After a careful basic characterization, devices were shipped to Linz, Austria, where devices were packaged using a UV-curable epoxy (Ossila E131) and thin glass slides. Thin copper wires were attached to the gold electrodes using small indium pads. Photovoltaic performance was evaluated using commercial solar simulators. The light intensity was matched to 1 sun (AM 1.5G or 100 mW cm^{-2}) by calibration with a Si reference cell. Current–voltage (J–V) curves were collected by applying an external bias voltage while measuring the current response using a Keithley 2400 source meter unit.

External quantum efficiencies (EQEs) were recorded using a lock-in amplifier (SR830, Stanford Research Systems) and a variable gain preamplifier (Jaissle 1002 potentiostat or FEMTO DLPCA-200). Solar cells were illuminated by monochromatic light from a white light lamp passing through a monochromator with typical intensities in the range of 0.1–10 μW. A set of long-pass filters and a mechanical chopper were mounted between the lamp and the monochromator. Chopping frequencies in the range of 113–273 Hz were used. A calibrated silicon (Hamamatsu S2281) and a calibrated InGaAs diode (Hamamatsu G12180) were used as references.

The electroluminescence quantum yield was determined using a calibrated external quantum efficiency measurement system (Hamamatsu C9920-12). The system comprises an integrating sphere, a photonic multichannel analyzer (Hamamatsu PMA-12 C10027-02), and a Keithley 2400 source meter unit. A schematic drawing of the experimental setup is shown in the Supporting Information (Figure S1, Supporting Information). For photoluminescence (PL) measurements, the light collected by the same integrating sphere was fed into a Shamrock monochromator (303-i) equipped with an iDus420 CCD camera. For photoluminescence measurements, long-pass filters were used to block the high-energy photons from the excitation source.

Supporting Information

Supporting Information is available from the Wiley Online Library or from the author.

Conflict of Interest

The authors declare no conflict of interest.

[1] M. A. Green, H. Yoshihiro, E. D. Dunlop, D. H. Levi, J. H. Ebinger, M. Yoshita, A. W. Y. Ho-Baillie, *Prog. Photovoltaics Res. Appl.* **2019**, *27*, 3.

[2] A. Kojima, K. Teshima, Y. Shirai, T. Miyasaka, *J. Am. Chem. Soc.* **2009**, *131*, 6050.

[3] A. Priyadarshi, L. J. Haur, P. Murray, D. Fu, S. Kulkarni, G. Xing, T. C. Sum, N. Mathews, S. G. Mhaisalkar, *Energy Environ. Sci.* **2016**, *9*, 3687.

[4] G. Grancini, C. Roldan-Carmona, I. Zimmermann, E. Mosconi, X. Lee, D. Martineau, S. Narbey, F. Oswald, F. De Angelis, M. Graetzel, M. K. Nazeeruddin, *Nat. Commun.* **2017**, *8*, 1.

[5] D. Liu, T. L. Kelly, *Nat. Photonics* **2014**, *8*, 133.

[6] M. Kaltenbrunner, G. Adam, E. D. Głowacki, M. Drack, R. Schwödiauer, L. Leonat, D. H. Apaydin, H. Groiss, M. C. Scharber, M. S. White, N. S. Sariciftci, S. Bauer, *Nat. Mater.* **2015**, *14*, 1032.

[7] G. E. Eperon, V. M. Burlakov, A. Goriely, H. J. Snaith, *ACS Nano* **2014**, *8*, 591.

[8] B. Conings, J. Drijkoningen, N. Gauquelin, A. Babayigit, J. D'Haen, L. D'Olieslaeger, A. Ethirajan, J. Verbeeck, J. Manca, E. Mosconi, *Adv. Energy Mater.* **2015**, *5*, 1500477.

[9] W. Nie, J.-C. Blancon, A. J. Neukirch, K. Appavoo, H. Tsai, M. Chhowalla, M. A. Alam, M. Y. Sfeir, C. Katan, J. Even, S. Tretiak, J. J. Crochet, G. Gupta, A. D. Mohite, *Nat. Commun.* **2016**, *7*, 11574.

[10] Y. Han, S. Meyer, Y. Dkhissi, K. Weber, J. M. Pringle, U. Bach, L. Spiccia, Y.-B. Cheng, *J. Mater. Chem. A* **2015**, *3*, 8139.

[11] C. C. Stoumpos, D. H. Cao, D. J. Clark, J. Young, J. M. Rondinelli, J. I. Jang, J. T. Hupp, M. G. Kanatzidis, *Chem. Mater.* **2016**, *28*, 2852.

[12] Y. Yang, F. Gao, S. Gao, S.-H. Wei, *J. Mater. Chem. A* **2018**, *6*, 14949.

[13] G. Grancini, M. K. Nazeeruddin, *Nat. Rev. Mater.* **2019**, *4*, 4.

[14] C. Ma, C. Leng, Y. Ji, X. Wei, K. Sun, L. Tang, J. Yang, W. Luo, C. Li, Y. Deng, S. Feng, J. Shen, S. Lu, C. Du, H. Shi, *Nanoscale* **2016**, *8*, 18309.

[15] J. Yan, W. Qiu, G. Wu, P. Heremans, H. Chen, *J. Mater. Chem. A* **2018**, *6*, 11063.

[16] J. Chen, J.-Y. Seo, N.-G. Park, *Adv. Energy Mater.* **2018**, *8*, 1702714.

[17] K. Yao, X. Wang, F. Li, L. Zhou, *Chem. Commun.* **2015**, *51*, 15430.

[18] K. T. Cho, G. Grancini, Y. Lee, E. Oveisi, J. Ryu, O. Almora, M. Tschumi, P. A. Schouwink, G. Seo, S. Heo, J. Park, J. Jang, S. Paek, G. Garcia-Belmonte, M. K. Nazeeruddin, *Energy Environ. Sci.* **2018**, *11*, 952.

[19] U. Rau, *Phys. Rev. B* **2007**, *76*, 085303.

[20] Z. Liu, L. Krückemeier, B. Krogmeier, B. Klingebiel, J. A. Márquez, S. Levcenko, S. Öz, S. Mathur, U. Rau, T. Unold, T. Kirchartz, *ACS Energy Lett.* **2019**, *4*, 110.

[21] Q. Jiang, Y. Zhao, X. Zhang, X. Yang, Y. Chen, Z. Chu, Q. Ye, X. Li, Z. Yin, J. You, *Nat. Photonics* **2019**, DOI: 10.1038/s41566-019-0398-2.

[22] G. Adam, M. Kaltenbrunner, E. D. Glowacki, D. H. Apaydin, M. S. White, H. Heilbrunner, S. Tombe, P. Stadler, B. Ernecker, C. W. Klampfl, N. S. Sariciftci, M. C. Scharber, *Sol. Energy Mater. Sol. Cells* **2016**, *157*, 318.

[23] Z. Hameiri, A. M. Soufiani, M. K. Juhl, L. Jiang, F. Huang, Y.-B. Cheng, H. Kampwerth, J. W. Weber, M. A. Green, T. Trupke, *Prog. Photovoltaics Res. Appl.* **2015**, *23*, 1697.

[24] D. Walter, Y. Wu, T. Duong, J. Peng, L. Jiang, K. C. Fong, K. Weber, *Adv. Energy Mater.* **2018**, *8*, 1701522.

[25] P. Wurfel, *J. Phys. C Solid State Phys.* **1982**, *15*, 3967.

[26] L. Lombez, M. Soro, A. Delamarre, N. Naghavi, N. Barreau, D. Lincot, J.-F. Guillemoles, *J. Appl. Phys.* **2014**, *116*, 064504.

[27] D. Shvydka, V. G. Karpov, A. D. Compaan, *Appl. Phys. Lett.* **2002**, *80*, 3114.

[28] I. E. Beckers, U. Fiedeler, S. Siebentritt, M. C. Lux-Steiner, *J. Phys. Chem. Solids* **2003**, *64*, 2031.